Geophys. J. Int. (2007) doi: 10.1111/j.1365-246X.2007.03414.x

Ambient noise Rayleigh wave tomography of New Zealand

Fan-Chi Lin[1], Michael H. Ritzwoller[1], John Townend[2], Stephen Bannister[3] and Martha K. Savage[2]

[1] *Center for Imaging the Earth's Interior, Department of Physics, University of Colorado at Boulder, Boulder,* CO 80309-0390*, USA. E-mail: linf@ciei.colorado.edu*

[2] *Institute of Geophysics, School of Geography, Environment, and Earth Sciences, Victoria University of Wellington,* PO Box 600*, Wellington* 6040*, New Zealand*

[3] *GNS Science,* PO Box 30368*, Lower Hutt* 6315*, New Zealand*

Accepted 2007 February 21. Received 2007 February 20; in original form 2006 August 30

SUMMARY

We present the first New Zealand-wide study of surface wave dispersion, using ambient noise observed at 42 broad-band stations in the national seismic network (GeoNet) and the Global Seismic Network (GSN). Year-long vertical-component time-series recorded between 2005 April 1 and 2006 March 31 have been correlated with one another to yield estimated fundamental mode Rayleigh wave Green's functions. We filter these Green's functions to compute Rayleigh wave group dispersion curves at periods of 5–50 s, using a phase-matched filter, frequency–time analysis technique. The uncertainties of the measurements are estimated based on the temporal variation of the dispersion curves revealed by 12 overlapping 3-month stacks. After selecting the highest quality dispersion curve measurements, we compute group velocity maps from 7 to 25 s period. These maps, and 1-D shear wave velocity models at four selected locations, exhibit clear correlations with major geological structures, including the Taranaki and Canterbury Basins, the Hikurangi accretionary prism, and previously reported basement terrane boundaries.

Key words: ambient noise, cross-correlations, crustal structure, New Zealand, surface waves, tomography.

1 INTRODUCTION

Surface wave tomography has proven to be very useful in imaging the crust and uppermost mantle on both regional and global scales across much of the globe. Surface waves of different periods are sensitive to seismic shear wave speeds at different depths, with the longer period waves exhibiting sensitivity to greater depths. By measuring the dispersive character of surface waves, strong constraints can be placed on the shear wave velocity structure of the crust and upper mantle.

Observations of diffuse seismic wavefields (namely ambient noise and scattered coda waves) alleviate some of the problems affecting traditional surface wave measurements made on teleseismic earthquake recordings. Recent theoretical work has revealed that under the assumption that the sources of the ambient noise are evenly distributed, the Green's function between two points can be estimated from the cross-correlatation of recordings made at the two locations (Weaver & Lobkis 2001a,b, 2004; Derode *et al.* 2003; Snieder 2004; Wapenaar 2004; Larose *et al.* 2005). Snieder (2004) showed that only the sources near the line connecting two stations will contribute to the signals observed in the cross-correlation function. Sources at opposite sides of the line will contribute to the signal at positive and negative lags in the cross-correlation function respectively. Results of using diffuse seismic wavefields to extract the Green's function have been substantiated using earthquake coda waves (Campillo & Paul 2003; Paul *et al.* 2005) and ambient seismic noise for surface waves (e.g. Shapiro & Campillo 2004; Sabra *et al.* 2005a) and local body waves (Roux *et al.* 2005).

The scientific appeal of ambient noise imaging lies in using pervasive and continuous seismic energy to map subsurface shear wave velocities over large areas (e.g. Shapiro *et al.* 2005). Ambient seismic noise correlation has been applied successfully to data recorded by instruments in Southern California to produce high-resolution tomographic surface wave group velocity maps at periods of 7.5–15 s (Shapiro *et al.* 2005; Sabra *et al.* 2005b). These velocity maps exhibit striking correlations with the regional geological structure: low-speed anomalies correspond to the major sedimentary basins, and high-speed anomalies to the cores of the Sierra Nevada and other mountain ranges (Shapiro *et al.* 2005). Yang *et al.* (2007) demonstrated that similar results can be obtained at larger scales and longer periods across much of Europe. Other applications have arisen with the growth of the Transportable Array component of EarthScope being tracked across California and the Pacific Northwest (Moschetti *et al.* 2005), in South Korea at very short periods (Cho *et al.* 2007), in Tibet at long periods (Yao *et al.* 2006) and elsewhere. Note that while most studies to date have been conducted in continental settings, oceanic applications of ambient noise correlation at very large scales also appear to be feasible (Lin *et al.* 2006).

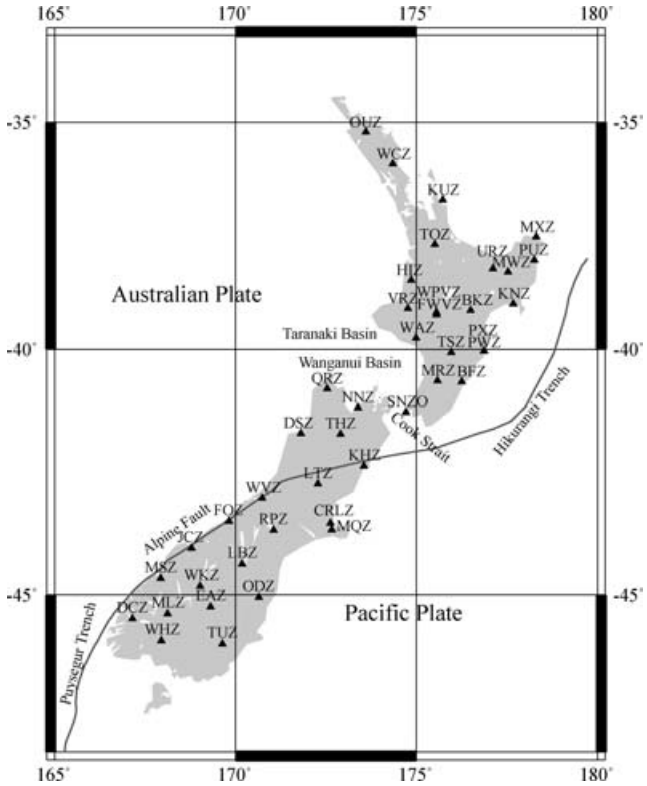

Figure 1 The seismic stations used in this study: 41 stations from the New Zealand GeoNet Project and one (SNZO) from the Global Seismic Network (Butler *et al.* 2004).

New Zealand is a prime target for ambient noise surface wave tomography. It is now spanned by a modern broadband seismological network (GeoNet, Fig. 1) and is surrounded on all sides by sea. This oceanic isolation, which subjects it to some of the most sustained and energetic ocean waves on Earth (e.g. Laing *et al.* 2000; Gorman *et al.* 2003), creates very high ambient noise levels that can be exploited for tomography. The high noise levels may provide more uniform illumination of the crust than in other continental locations where ambient noise imaging has been undertaken. Furthermore, the varied tectonic environments in New Zealand provide strong lateral variations in seismic wave speeds, and the findings of numerous regional studies, referred to below, are available for comparison with the noise analysis results.

New Zealand's tectonic architecture encompasses a variety of tectonic deformation styles, including subduction, rifting and transpression. Such different tectonic environments are expected to yield strong lateral and vertical variations in shear wave structure that are amenable to imaging with surface waves. Yet few studies of surface waves in New Zealand have been undertaken to date. This is due in part to the historical shortage of broadband seismic stations in New Zealand (a situation largely rectified now with the advent in 2001 of the GeoNet project, http://www.geonet.org.nz/). More fundamentally, it stems from basic limitations suffered by earthquake-based surface wave tomography. In particular, previous surface wave dispersion measurements in regions like New Zealand with relatively low levels of seismicity have been based almost exclusively on teleseismic earthquakes. It is difficult to obtain reliable short-period (<20 s) dispersion measurements from distant earthquakes due to intrinsic attenuation and scattering along ray paths, and it is these short-period waves that are most useful for constraining the structure of the crust and uppermost mantle. Moreover, surface wave sensitivity functions for teleseismic events are spatially broad, which limits the lateral resolution. For these reasons, the long history of multidisciplinary research on the structure and tectonics of New Zealand (see recent publications by Davey 1998; Stern *et al.* 2000; Okaya *et al.* 2002; Scherwath *et al.* 2002; Savage *et al.* 2004; Baldock & Stern 2005; Reyners *et al.* 2006; Stern *et al.* 2006) has involved little systematic investigation or use of seismic surface waves. The most detailed work in New Zealand to date on surface wave dispersion was undertaken by Brisbourne and co-workers (Brisbourne & Stuart 1998; Brisbourne *et al.* 1999), who investigated the shear wave velocity of the eastern North Island based on fundamental Rayleigh wave phase velocities at 17–73 s period using teleseismic observations of four earthquakes. Surface wave observations and receiver functions have also been used recently to study the shear wave structure of the northernmost North Island (Horspool *et al.* 2006).

In this paper we apply ambient noise tomography between 7 and 25 s period to 42 broad-band seismic stations distributed almost evenly across the North and South Islands of New Zealand (Fig. 1), using methods described by Bensen *et al.* (2007) and outlined in Section 2. One of the principal benefits of ambient noise tomography over traditional earthquake tomography is the ability to estimate measurement uncertainties based on the repeatability of the measurements. The error analysis and its use in identifying reliable measurements are described in Section 3. The results of group speed tomography between periods of 8 and 23 s are presented in Section 4 and discussed in Section 5 in terms of New Zealand's regional geology. We close Section 5 with a brief illustration of the apparent azimuthal distribution of the ambient noise sources that underpin the noise correlation method.

2 DATA PROCESSING AND GROUP VELOCITY MEASUREMENTS

We have analysed continuous broad-band vertical-component seismic data spanning the period from 2005 April 1 to 2006 March 31 recorded by 42 stations in the GeoNet national network and the Global Seismic Network (GSN; Fig. 1). The exclusive use of vertical-component data limits the subsequent analysis to Rayleigh waves. Bensen *et al.* (2007) discuss at length the data processing scheme that precedes ambient noise tomography and we make only minor modifications here.

The data are processed one day at a time in single-station and station-pair steps. First, single station processing begins by removing the daily trend, mean, and instrument response from each record to create raw velocity seismograms. Next, unwanted events such as earthquake signals and instrumental irregularities (spikes) are removed by what Bensen *et al.* (2007) refer to as 'temporal normalization'. Earthquakes occur regularly throughout much of New Zealand and north of the country along the Tonga-Kermadec trench, in particular, and cross-correlations of raw data tend to be contaminated by any earthquakes represented in the data. We undertake temporal normalization to ameliorate the otherwise contaminating effects of earthquakes on the noise correlations. During this step, the raw velocity seismograms are first bandpass filtered to 15–50 s periods. This band contains the most energetic surface waves arriving after earthquakes. Then the absolute value of these filtered seismograms are smoothed with a 128 s-duration moving window to provide the envelope functions. These envelope functions are largest near the times containing earthquake signals. The 5–100 s period

bandpass-filtered raw velocity seismograms are then weighted by the inverse of the envelope functions to complete the temporal normalization process. This provides 5–100 s period seismograms with suppressed earthquake signals and has proven to be more robust than the more time-consuming process of simply removing signals where large earthquakes are known to have occurred. Bensen *et al.* (2007) provide further details of how tuning the temporal normalization to regional earthquake characteristics helps to diminish unwanted signals in the correlations further.

The temporally normalized signals are next whitened in the frequency domain. This completes the single-station preparation, after which the day-long waveform at each station is correlated with that at each of the other stations and the daily results are added together to produce one 12-month stack and twelve 3-month stacks. As the cross-correlation and stacking processes are linear, it does not matter whether the waveforms are stacked in single days or longer or shorter time intervals. The 3-month stacks are used to estimate the uncertainty in each dispersion measurement, as discussed further in the Section 3.

Fig. 2 shows an example of 12-month stacks of broadband (5–100 s) cross-correlations plotted as a record-section with respect to station BFZ (Birch Farm). Clear signals are seen for both positive and negative correlation lags with physically reasonable moveouts (2–3 km s^{-1}). The signals at positive and negative lags represent waves travelling in opposite directions: they sample the same media and are expected to exhibit the same velocities and dispersion characteristics. For this reason, we average the positive- and negative-lag signals by averaging the cross-correlation with its time inversion to form what we refer to below as the 'symmetric-component'. Fig. 3 displays positive lags of 12-month symmetric-component cross-correlations between stations Denniston North (DSZ) and Hauiti (HIZ) for different period bands (negative lags are identical to the positive lags). The earlier arrivals at longer periods result from normal dispersion of the signals in which longer periods travel faster than shorter periods. Fig. 4(a) compares a broadband cross-correlation with its symmetric-component for stations Earnscleugh (EAZ) and Top House (THZ).

As in earthquake dispersion analysis (e.g. Ritzwoller & Levshin 1998), the dispersion measurement applied to ambient noise cross-correlations is based on frequency–time analysis (FTAN) in a two-step process applied to the cross-correlation between data from each pair of stations. However, the procedure applied here is automated, whereas the earthquake analysis typically involves manual intervention by an analyst. Bensen *et al.* (2007) discuss the dispersion measurement procedures used in this paper in greater detail, and here we provide only a brief summary. The first phase of traditional FTAN involves the construction of a 2-D diagram of signal power as a function of time or group velocity and the central frequency or period of successive narrow-band Gaussian filters (Fig. 4c). The automatic procedure used here tracks the local power maximum along the period axis. The group arrival times of the maximum amplitude as a function of filter period are used to calculate a preliminary (raw) group velocity curve. Formal criteria are used to identify and reject curves with distinctly irregular behaviour or to interpolate through small spectral holes by selecting realistic local rather than absolute maxima. The second part of the FTAN method is the application of a phase-matched or antidispersion filter (Fig. 4d). In the non-automated method that has been applied to large numbers of earthquake records previously, the analyst defines both the phase-matched filter and the frequency band of the measurement. In the automated method employed here, the frequency band of interest is pre-set and the phase-matched filter is defined by the dispersion curve identified in the first step of the analysis. In both the manual and automated analyses, the actual frequency of a given filter is found from the time derivative of the phase at selected amplitude maxima (Levshin & Ritzwoller 2001). Bensen *et al.* (2007) also discuss the use of similar means to measure phase velocities, but only group velocities are considered here.

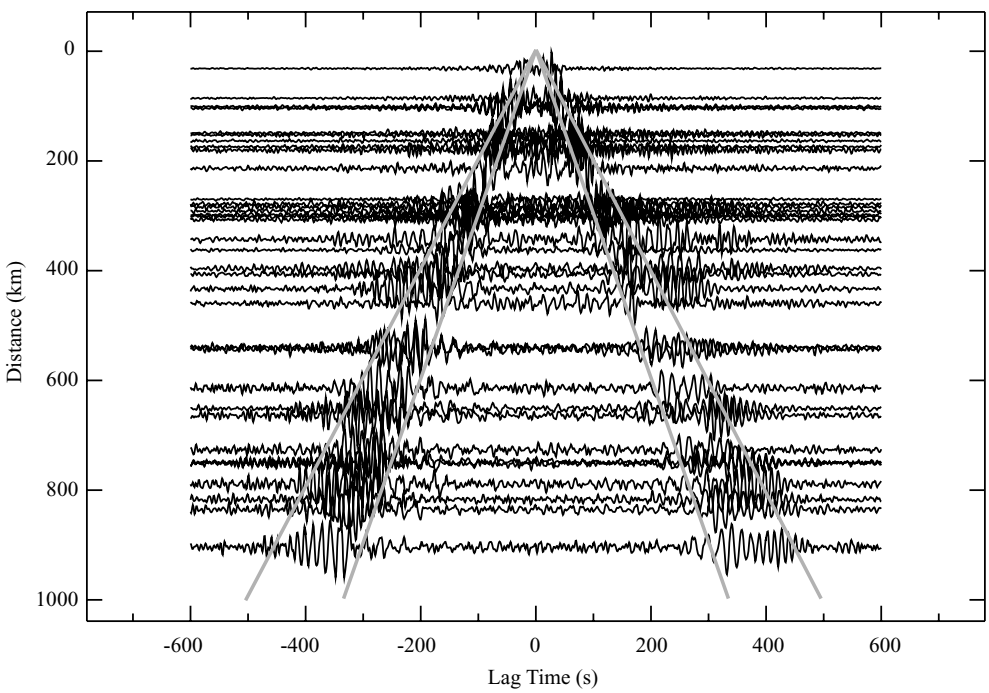

Figure 2 A broadband (5–100 s period) record section centred at station BFZ (Birch Farm, eastern Wairarapa, New Zealand). Both positive ('causal') and negative ('acausal') lags are shown. The gray lines mark 'moveout' at velocities of 2 and 3 km s^{-1}.

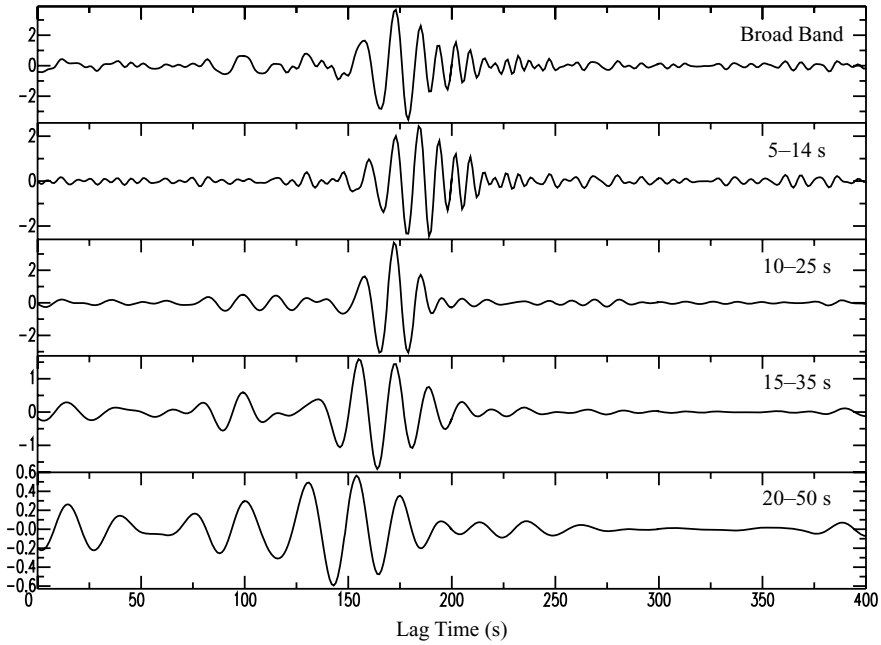

Figure 3 One-year stack of the symmetric-component cross-correlation signal observed for the station-pair DSZ–HIZ (Denniston North and Hauiti) filtered into various period bands.

We depart from the method of analysis advocated by Bensen *et al.* (2007) in that for data from New Zealand we can increase the number of measurements by performing the FTAN and phase-matched filtering procedures in four overlapping period bands (5–14, 10–25, 15–35 and 20–50 s). This is because in spite of applying spectral whitening to the single-station data, the spectra of the correlation signals are not completely white, but are stronger in some bands than others. Breaking the dispersion analysis into sub-bands after cross-correlation more effectively flattens the amplitude spectra and improves the measurements in many cases. The dispersion curves at the edges of each period band, however, do not match perfectly nor do the FTAN diagrams, as evidenced by the precursory artefact at about 20 s period in Fig. 4(d). The choice of overlapping period bands allows us to eliminate the measurements that suffer from edge effects. At periods for which we have two measurements we use the group velocities with lower average uncertainty. We discuss this further in Section 3.

Figs 5(b) shows group speed curves between stations DCZ and LTZ, OUZ and QRZ, KHZ and ODZ and PXZ and WCZ along paths through four distinct geological regions (Fig. 5a). As noted above, the curves do not meet seamlessly between the four frequency bands in which they are measured, but off-sets tend to be small. In general, a Rayleigh wave samples to a depth of approximately one-third its wavelength. Low wave speeds at short periods ($<$15 s) usually indicate sediments near the surface and high wave speeds usually are associated with the intracrustal roots of mountain ranges or metamorphic terranes. The lowest wave speeds at short periods in Fig. 5(b) for path OUZ–QRZ are due to offshore sediments. At longer periods, waves begin to sample the upper mantle and a relatively short period onset of high group speeds is related to thin crust because the high-speed mantle is nearer to the surface. In general, both the on-set of rising and the slope of the dispersion curve from about 20 to 30 s period provides information about both crustal thickness and upper mantle shear velocity. Note that the DCZ–LTZ path is through the Southern Alps, an area considered to have the thickest crust in New Zealand (e.g. Eberhart-Phillips & Bannister 2002), and has the flattest group speed curves at 20–30 s periods. The significance of these features is discussed in Section 5.

3 ERROR ANALYSIS AND DATA SELECTION

The automated measurement procedure must be accompanied by the application of criteria that identify the most reliable measurements. There are four such criteria: (1) a period cut-off related to inter-station distance, (2) signal-to-noise ratio (SNR), (3) repeatability of the measurements (particularly seasonal variability) and (4) coherence across the set of measurements. The formal uncertainty analysis is based on seasonal variability.

First, for closely spaced station-pairs, the signals at positive and negative lags can interfere with spurious precursory arrivals and each other at long periods, rendering the measurements unreliable. This effect can be mitigated by introducing a period cut-off in which measurements are accepted only if the inter-station distance is greater than $\sim$3 wavelengths. A typical phase speed of $\sim$4 km s^{-1} provides a rule-of-thumb that we accept a measurement only below the cut-off period of $\Delta/12$ seconds, where Δ is the inter-station distance in kilometres. Experience shows that this is near the period at which measurements begin to deteriorate, being less repeatable and more subject to changes associated with small variations in the measurement process. The KHZ–ODZ measurement in Fig. 5(b), for example, cuts off at a period of about 33 s.

Second, the quality of the dispersion measurement is highly correlated with the signal-to-noise ratio (SNR) of the cross-correlation. We compute spectral SNR by applying a series of narrow bandpass filters and measuring signal-to-noise levels after returning to the time-domain. The signal level is defined as the peak amplitude in the arrival window and the noise level as the root mean square (rms) noise in the noise window, where the arrival window spans the interval from 75 s before until 75 s after the expected Rayleigh wave group times taken from the 3-D model of Shapiro and Ritzwoller

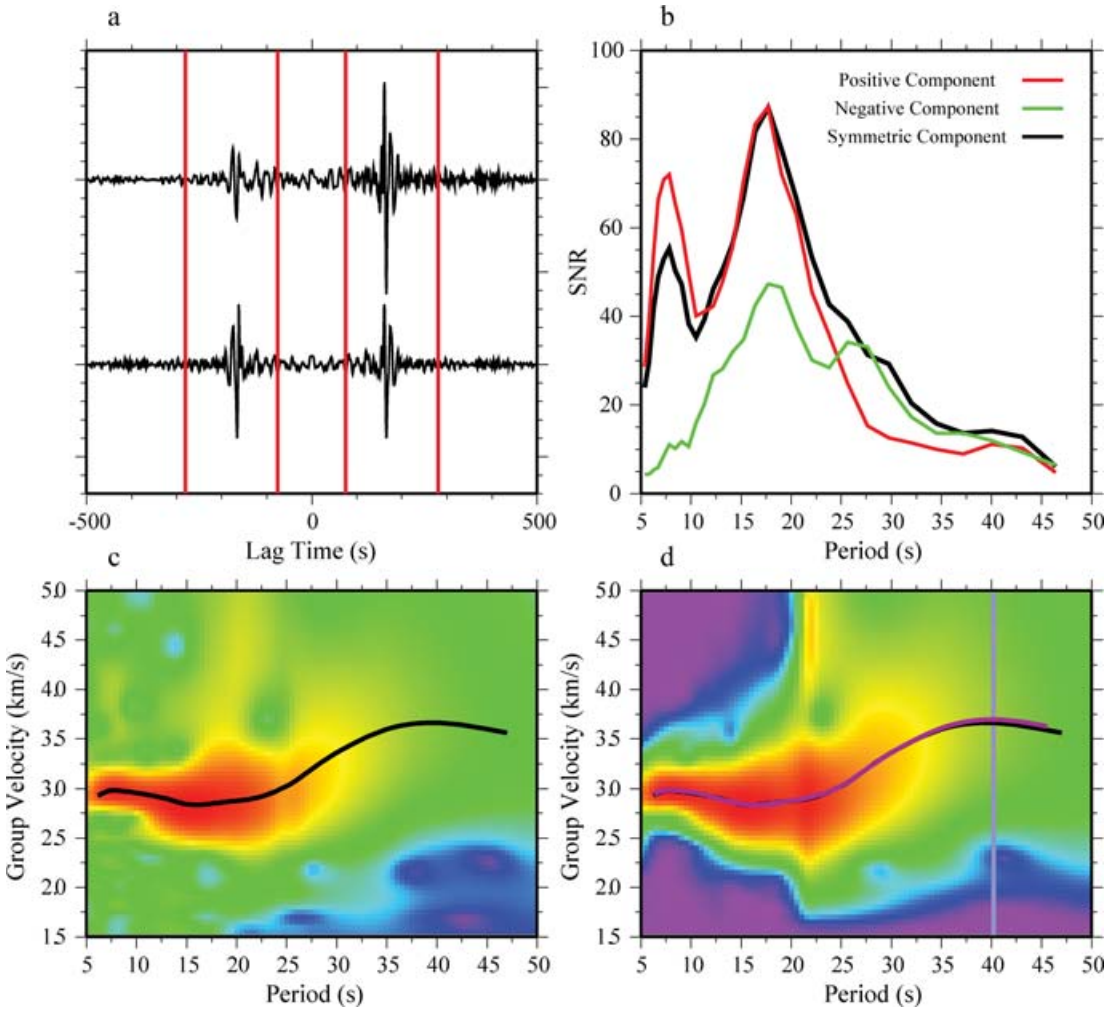

Figure 4 (a) One-year cross-correlation between stations EAZ (Earnscleugh) and THZ (Top House) showing the window defining the signal location outlined in red. The cross-correlation is the top waveform and the symmetric-component waveform is shown below it. (b) The spectrum of the signal-to-noise ratio of the positive (red) and negative (green) lags of the cross-correlation and the symmetric-component (black) shown in (a). (c) Frequency-time image of the symmetric-component shown in (a) and the measured raw group-speed curve, where warm colours indicate larger amplitudes. (d) Frequency-time image after phase-matched filtering based on the raw dispersion measurement. The black line is the raw dispersion measurement from (c), the magenta line is the group speed measurement from phase-matched filtering, and the vertical blue line is the cut-off period below which waves travelled more than three wavelengths between the two stations.

(2002) at the minimum and maximum periods of the passband. The noise window starts 500 s after the end of the signal window and ends at 2700 s lag time. Fig. 4(b) shows examples of spectral SNR for the positive and negative lag signals in Fig. 4(a) and the corresponding symmetric-component. With extreme asymmetry (e.g. in Fig. 4b, at periods of <10 s), the symmetric-component SNR can be degraded by the lag containing the weaker signal. However, in general, the symmetric-component has a better or at least comparable SNR relative to a single lag (Fig. 4b, at periods >10 s), which is why we use it to obtain the dispersion measurements rather than using one of the two lags. The SNR is typically highest at the New Zealand stations below periods of about 20 s (the microseism band) and deteriorates rapidly at periods above about 25 s. This is one reason why the analysis in this paper concentrates on periods below 30 s, the other being that measurements at longer periods require an interstation spacing exceeding 360 km. Such long paths lie exclusively along the strike of New Zealand, and therefore azimuthal coverage above about 20 s period is poorer than at shorter periods for which more interstation paths exist, particularly paths that lie transverse to the strike of the country.

Third, we require that a measurement be repeatable in order to use it for tomography. To quantify repeatability, we measure the seasonal variability of each measurement and then equate this with the measurement uncertainty. To compute seasonal variability, we use the twelve 3-month stacks represented in the data (Apr05–May05–Jun05, May05–Jun05–Jul05, . . . , Mar06–Apr05–May05; i.e. assuming annual periodicity) in our data set and the dispersion curves measured on each of them (Fig. 6). At each period and for each pair of stations, we consider a measurement potentially reliable if there are more than seven 3-month stacks with a SNR value higher than 15. We then compute the standard deviation (SD) of the group speeds and arrival times using the 3-month stacks meeting this condition. We screen out all the station-pairs with either a group speed SD higher than 100 m s^{-1} or an arrival time SD exceeding 4 s. In general, station-pairs with long distance are selected by the arrival time SD criterion and station-pairs with short distance are selected

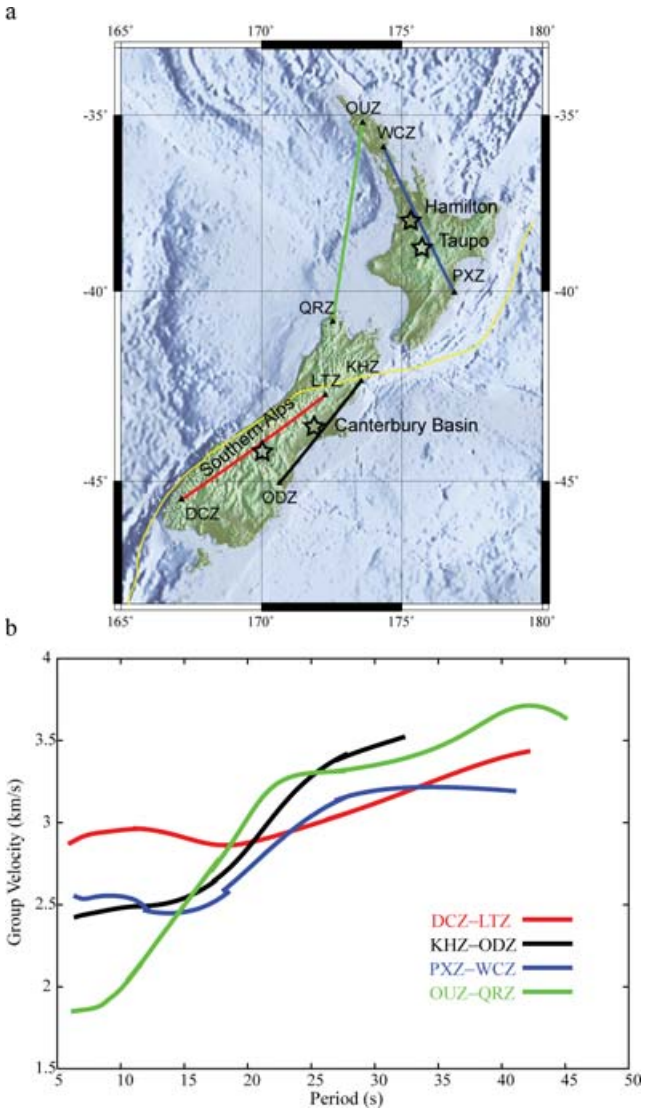

Figure 5 (a) Interstation paths for the group speed measurements shown in (b). Paths through: an offshore basin (OUZ–QRZ; Omahuta and Quartz Range), the Southern Alps (DCZ–LTZ; Deep Cove and Lake Taylor Station), the eastern side of the South Island (KHZ–ODZ; Kahutara and Otahua Downs), and the North island (PXZ–WCZ; Pawanui and Waipu Caves). The colour codes in (a) and (b) are the same. Four locations, Hamilton, Taupo, Canterbury Basin and Southern Alps, where we invert for 1-D models in Section 5.2 are marked as stars here.

by the speed SD criterion. The group velocity SD averaged overall station pairs for the four period bands we use in the dispersion measurement process are plotted in Fig. 7. The uncertainties increase at the edges of each period band. As noted above, at periods spanned by more than one analysis band, the data from the band giving the smaller uncertainty are chosen. For example, at 21 s period, the 15–35 s-band measurement yields the lower average SD group velocity and is, therefore, chosen to provide the measurement at 21 s period.

The number of measurements that satisfy these criteria, the average SNR, the average group speed uncertainty, and the average arrival time uncertainty at each period are summarized in Fig. 8. Note that above 25 s period, very few measurements meet the selection criteria, which limits tomography to periods below this threshold. Although the average SNR peaks at a period of 16 s, the number of measurements maximizes at 15 s. This is mainly due to the competition between the number of measurements satisfying the distance and SNR criteria. Fig. 9 plots all the paths satisfying these criteria at 8, 13, 18 and 23 s periods. At the longer periods, the propagation paths are increasingly confined to the long axes of the North and South Islands due principally to the three-wavelength interstation spacing criterion. Paths orthogonal to the strike of the islands exist in fairly large numbers at 8 s period and also at 13 s period.

4. GROUP SPEED TOMOGRAPHY

The Rayleigh wave dispersion measurements from one-year cross-correlations are used to invert for group velocity maps at periods from 7 to 25 s on a 0.25° × 0.25° grid spanning onshore New Zealand and the surrounding region, using the tomographic method of Barmin *et al.* (2001). This method is based on minimizing a penalty functional composed of a linear combination of data misfit, model smoothness, and the perturbation $\mathbf{m}$ to a reference model $\mathbf{m}_o$ for isotropic wave speed. The measurement uncertainties discussed in the previous section (SD of group velocities) are incorporated in the inversion and in regions of poor data coverage the estimated model blends smoothly into the reference model. No adequate crustal reference model exists on the scale of this experiment, so we have used the average of the measurements at each period to define the reference model $\mathbf{m_0}$. A more detailed discussion of this method is given by Barmin *et al.* (2001) and a recent application can be found in Yang *et al.* (2007).

Damping parameters weight the relative influence of data fit, smoothing, and tendency to merge the estimated model into the background model, and the choice of these parameters is somewhat subjective. We perform a series of tests using different combinations of these parameters to determine acceptable values by considering data misfit, model resolution and model norm. Ray theory is used to compute the surface wave traveltimes, albeit the ray theory we use is actually Gaussian beams with widths increasing with period. In recent years, surface wave studies have increasingly used diffraction tomography based on spatially extended finite-frequency sensitivity kernels derived from the Born/Rytov approximation (e.g. Spetzler *et al.* 2002; Ritzwoller *et al.* 2002; Yoshizawa & Kennett 2002; Zhou *et al.* 2004; many others). Based on the same ray theory as we use here, Ritzwoller *et al.* (2002) showed that diffraction tomography recovers similar structure to ray theory at periods shorter than 50 s in most continental regions with dense path coverage. Similarly, Sieminski *et al.* (2004) showed that nearly identical resolution is achieved with ray theory and finite-frequency theory. In this study, we only concentrate on short periods (<25 s) and on a region in which station coverage and the resulting ray paths are dense, so that ray theory with wide rays suffices for the surface wave tomography. Dahlen & Zhou (2006) caution that group delay tomography for group speeds suffers from a simultaneous sensitivity to phase speeds, but this poses a potential problem only at much longer periods than considered here.

Resolution is estimated using the method described by Barmin *et al.* (2001) with modifications presented by Levshin *et al.* (2005). Each row of the resolution matrix is a resolution surface (or kernel), which is a map defining the resolution at one spatial node. The shape of the resolution surface for most nodes resembles a 2-D spatial Gaussian function at periods shorter than 13 s. At periods longer than 13 s, paths with SW–NE direction dominate the paths used in the inversion and slightly SW–NE elongated resolution surfaces were observed. We summarize the information in the resolution surface by a single scalar quantity at each node, called

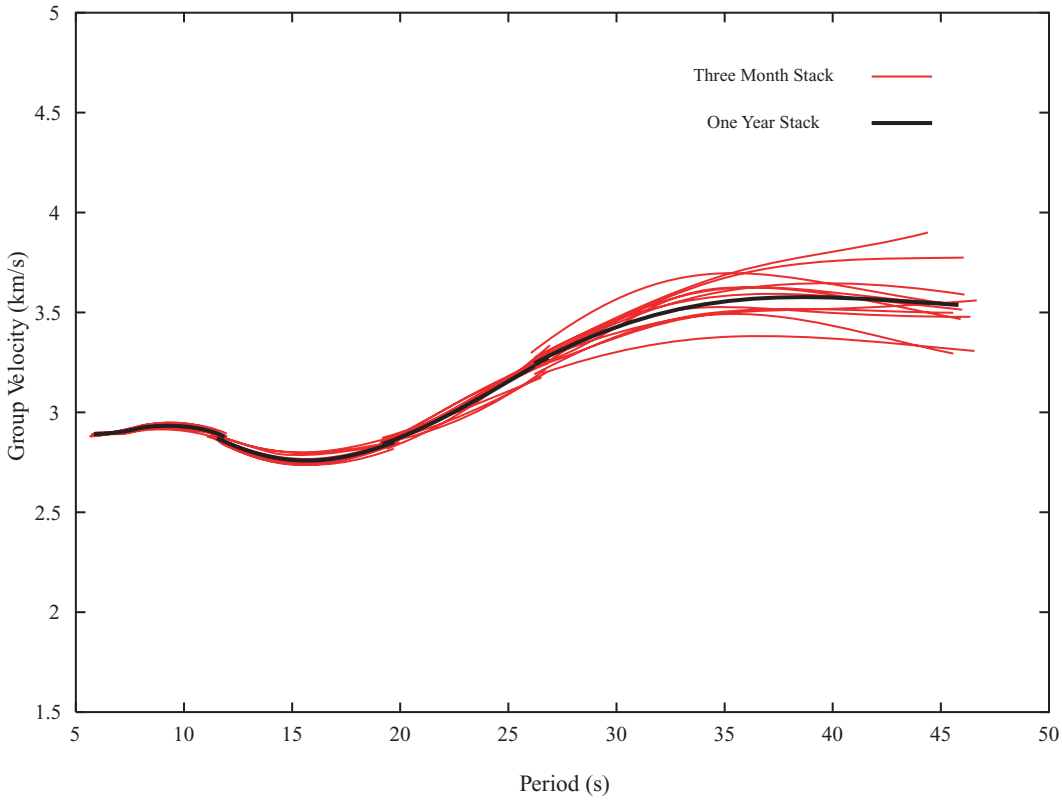

Figure 6 The measured group speed curves for twelve 3-month stacks are shown by red lines and the curve for the one-year stack is shown with a black curve for stations THZ (Top House) and TUZ (Tuapeka). The variation between the separate three-month stacks is used to estimate measurement uncertainties at each period.

the spatial resolution. We approximate the resolution surface at each node with the best-fitting 2-D symmetric spatial Gaussian function and represent the corresponding local spatial resolution with this Gaussian function's standard deviation. The resulting resolutions estimated across the region of study at periods of 8, 13, 18 and 23 s are shown in Fig. 10. We observe the resolution to be fairly constant at 8–18 s periods, with an average of 35 km on both islands, equating to approximately half the interstation spacing as expected for good data coverage. As expected, however, resolution deteriorates towards the coast of both main islands and because few measurement paths span the two islands at 8 s period, resolution in the vicinity of the Wanganui Basin and Cook Strait at 8 s is worse than at longer periods. At the longest period shown here, 23 s, horizontal resolution is uniformly worse (>45 km) than that at shorter periods because the total number of measurements is smaller and because, in particular, very few sufficiently long paths are oriented orthogonal to the country's predominant strike.

The tomographic results at 8, 13, 18 and 23 s periods are shown in Fig. 11. Rayleigh wave speeds in the South Island are typically faster than in the North Island. At 13 s period, the fastest speeds can be seen in the western South Island and wave speeds typically exhibit greater lateral variability in the North Island than the South Island. The lowest wave speeds are found offshore, west and east of the North Island: the western area corresponds to the Taranaki Basin, a major depocentre (King & Thrasher 1996). The eastern region includes the accretionary wedge in the Hikurangi subduction zone. The poorer resolution at 23 s period results in smoother tomographic features. Further discussion of the geological correlation of these features is given in Section 5.

The fits that the group speed maps provide to the data are shown in Fig. 12. These histograms show the misfit for all data meeting the first three selection criteria discussed in Section 3. The final step in the data selection process (Step 4 in Section 3) is intended to ensure that we use only those measurements that agree with the data set as whole. This involves iteratively rejecting badly fitting measurements. Measurements with misfit larger than 7 s, therefore, are removed prior to obtaining the final maps shown in Fig. 11. The first three steps in the data selection process account for the removal of nearly all the poor-quality measurements, and this final step removes only a few measurements and has only a minimal effect on the ultimate maps.

5 DISCUSSION

5.1 Geological interpretation of the group velocity maps

Many of the prominent features in the group velocity maps can be clearly associated with known geological structures (Fig. 13). In doing so, it is important to take each group velocity map's horizontal resolution and interstation path coverage into consideration, as well as the finite extent of the depth ranges sampled by surface waves. A fairly good rule-of-thumb is that the depth of maximum sensitivity of a group velocity is at its period expressed in kilometres. So, an 8 s group velocity measurement is predominantly sensitive to the top 8 km of the crust. The spatial smoothing used in constructing the tomographic images results in some instances of apparent velocity variations extending offshore (such as east of the North Island and

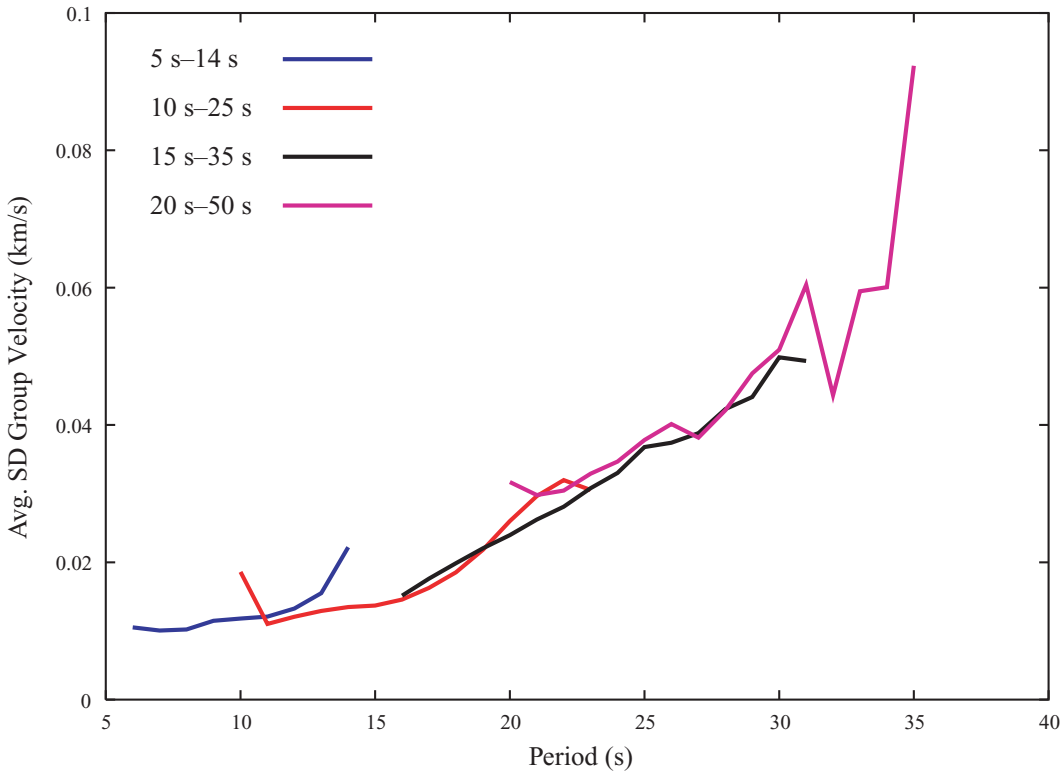

Figure 7 The group speed uncertainty (SD) averaged over all station pairs for each period band. For periods lying within two measurement bands, the band with the lowest average standard deviation is chosen to provide the group velocity measurement. The variation above 30 s period is mainly caused by the paucity of measurements.

west of the South Island, in the 18 s map), and care must be taken to avoid over-interpreting this leakage.

5.1.1 8 s group velocities

Low group velocities (<2.4 km s^{-1}) are observed west of the North Island, likely reflecting thick sedimentary deposits in the greater Taranaki Basin (TB, Fig. 13) offshore and to the west of Taranaki and Northland (Wood & Woodward 2002). The velocities change sharply across the west coast of Northland due to a change in sedimentary thickness across the Northland Boundary Fault (NBF, Fig. 13), which is located approximately 50 km offshore and parallel to the coastline (Uruski *et al.* 2004).

Low velocities are also observed along the east coast of the North Island, reflecting the presence of sedimentary basins up to 5 km deep in the Hikurangi subduction margin's accretionary prism (AP, Fig. 13; Beanland *et al.* 1998; Henrys *et al.* 2006). Similarly low velocities are observed in the Bay of Plenty, offshore north of the Taupo Volcanic Zone (TVZ, Fig. 13), where seismic reflection data reveal variable sediment thicknesses (Davey *et al.* 1995). The Taupo Volcanic Zone itself is rather poorly imaged at this period (*cf.* 13 s, below). Of perhaps more significance, however, is the fact that few station pairs exhibit high-SNR correlations at 8 s. This may be in part due to the noisy character of station TOZ in the Waikato region, which is addressed in Section 5.3, but the failure of stations MWZ, MXZ, PUZ and URZ to correlate well with HIZ at 8 s (Fig. 9) suggests strong attenuation of high-frequency energy within the Taupo Volcanic Zone, as also noted by Mooney (1970), Salmon *et al.* (2003) and Stern *et al.* (2006). Moreover, the apparent widening of the low-velocity areas off-shore here may simply represent a smearing out of the velocity structure along paths between Coromandel/Northland and East Cape.

The group velocities east of the North Island can be compared with recent wide-angle reflection and body-wave tomography (Henrys *et al.* 2006; Reyners *et al.* 2006). Henrys *et al.* (2006) quote values for V_p, V_p/V_s and Poisson's ratio of <5.5 km s^{-1}, >1.85 and >0.29, respectively, yielding $V_s < 3.0$ km s^{-1} for the uppermost 15 km of the crust in Hawke Bay. This suggests group velocity less than 2.5 km s^{-1} for periods below 10 s, which is compatible with the velocity found in our analysis.

The 8 s velocity map is much more homogeneous for the South Island. Velocities are predominantly >2.8 km s^{-1} other than in eastern Canterbury, where lower group velocities (<2.4 km s^{-1}) closely correspond to the position of the Canterbury Basin (CB, Fig. 13). A small region of low velocity is also observed in the northwest South Island (GID, Fig. 13), east of Westport. While the horizontal resolution and path coverage in this area are poorer than elsewhere in the inland South Island, we note that this location corresponds to sedimentary deposits in the Grey-Inangahua Depression (GID; Anderson 1979).

5.1.2 13 s group velocities

The key features of the 13 s group velocity map are broadly similar to those at 8 s. Once again, low surface wave velocities are imaged west of Northland and Taranaki. Onshore, velocities in Taranaki (Fig. 13) appear to increase abruptly eastwards, at a position close to the Taranaki Fault (TF, Fig. 13) and near the transition (Mortimer *et al.* 1997) between the Brook Strait and Murihiku basement terranes. Sherburn *et al.* (2006) identified a sharp east–west change in

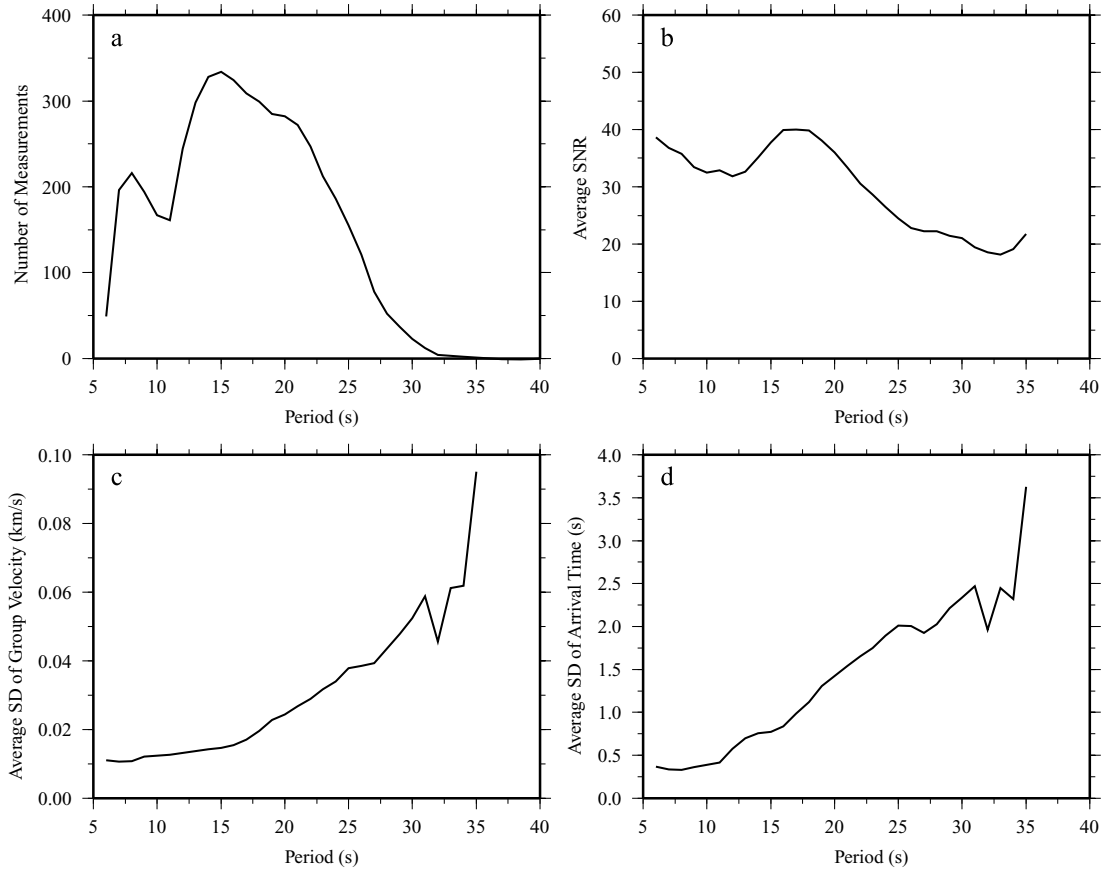

Figure 8 (a) The total number of group speed measurements at each period after completion of data selection. (b) The average of the SNR across all acceptable measurements for each period. (c) The average of the standard deviation (SD) of the group speed measurements among the 3-month stacks for each period, which is interpreted as the average measurement uncertainty. (d) As with (c), but for arrival times. Again, the variation above 30 s period mainly reflects the small number of measurements.

mid-crustal V_p values in the same location using a 3-D tomographic inversion of local earthquake traveltimes.

A band of higher group velocities (>2.9 km s^{-1}) is observed west of Wellington and appears to extend all the way from Cook Strait to Lake Taupo. The location of this band closely matches the interpreted extent of Haast schist in the southern North Island (Mortimer *et al.* 1997; Mortimer 2004). Schist outcrops at the surface in several locations, and is inferred to extend northwards from Cook Strait (starting at the offshore extension of the Wairau Fault), beneath the Wanganui Basin, to the Kaimanawa Ranges near Lake Taupo (Mortimer 1993; Mortimer *et al.* 1997). Laboratory velocity measurements on Haast schist by Godfrey *et al.* (2002) revealed mean (isotropic) *S*-wave velocities of 3.5–3.6 km s^{-1}.

In contrast to the low number of paths crossing the Taupo Volcanic Zone at 8 s periods, the area between Rotorua and Taupo appears to be reasonably well imaged at 13 s (Fig. 9). The low velocities in this region are compatible with the results of previous seismic studies in this region (e.g. Stern & Davey 1987; Harrison & White 2004; Stratford & Stern 2006) which indicate low *P*-wave velocities (<4 km s^{-1}) in the top 2–5 km. The ash and volcaniclastic sediments present in this area not only have intrinsically low seismic velocities, but are also strongly attenuating. Such attenuation has proven an impediment to previous active-source studies of the crust in this region (e.g. Stern 1987; Stratford & Stern 2006) and has itself been a focus of several studies (Hatherton 1970; Mooney 1970; Eberhart-Phillips & McVerry 2003; Salmon *et al.* 2003).

Consistently high velocities (>2.9 km s^{-1}) are found beneath the Southern Alps, from Fiordland as far north as the southern end of the Hope Fault. Slightly lower velocities (2.7–2.8 km s^{-1}) are found in Otago, and the Canterbury Basin sediments are still clearly distinguished (2.4–2.6 km s^{-1}). In the Canterbury-Otago region, Godfrey *et al.* (2001) observed a ∼5% difference in *P*-wave velocity at 10 km depth between the southern Canterbury Basin (<6 km s^{-1}) and offshore Otago and Southland (6.0–6.6 km s^{-1}), a comparable difference to that revealed by the 13 s Rayleigh wave speeds. To the west, seismic refraction measurements in Fiordland show *P*-wave velocities of 6.8 km s^{-1} within 3.5 km of the surface, and 7.3 km s^{-1} at a depth of about 8 km (Davey & Broadbent 1980).

5.1.3 18 s group velocities

Slow velocities (<2.6 km s^{-1}) are observed beneath the entire east coast of the North Island at 18 s period. Rayleigh waves of this period are likely to still be sampling the accretionary prism, but may also be influenced by the uppermost section of the subducted crust, especially along paths close to the coastline. The subducted plate is well imaged with local seismicity (Reyners *et al.* 2006) and deep seismic reflection data (Henrys *et al.* 2006): the subduction décollement dips northwest at 3°–6° and lies at a depth of ∼15 km (Davey *et al.* 1986; Ansell & Bannister 1996; Henrys *et al.* 2006) beneath the coastline immediately south of Hawke Bay. Higher velocities (>2.8 km s^{-1}) are observed in northwest Nelson (NN,

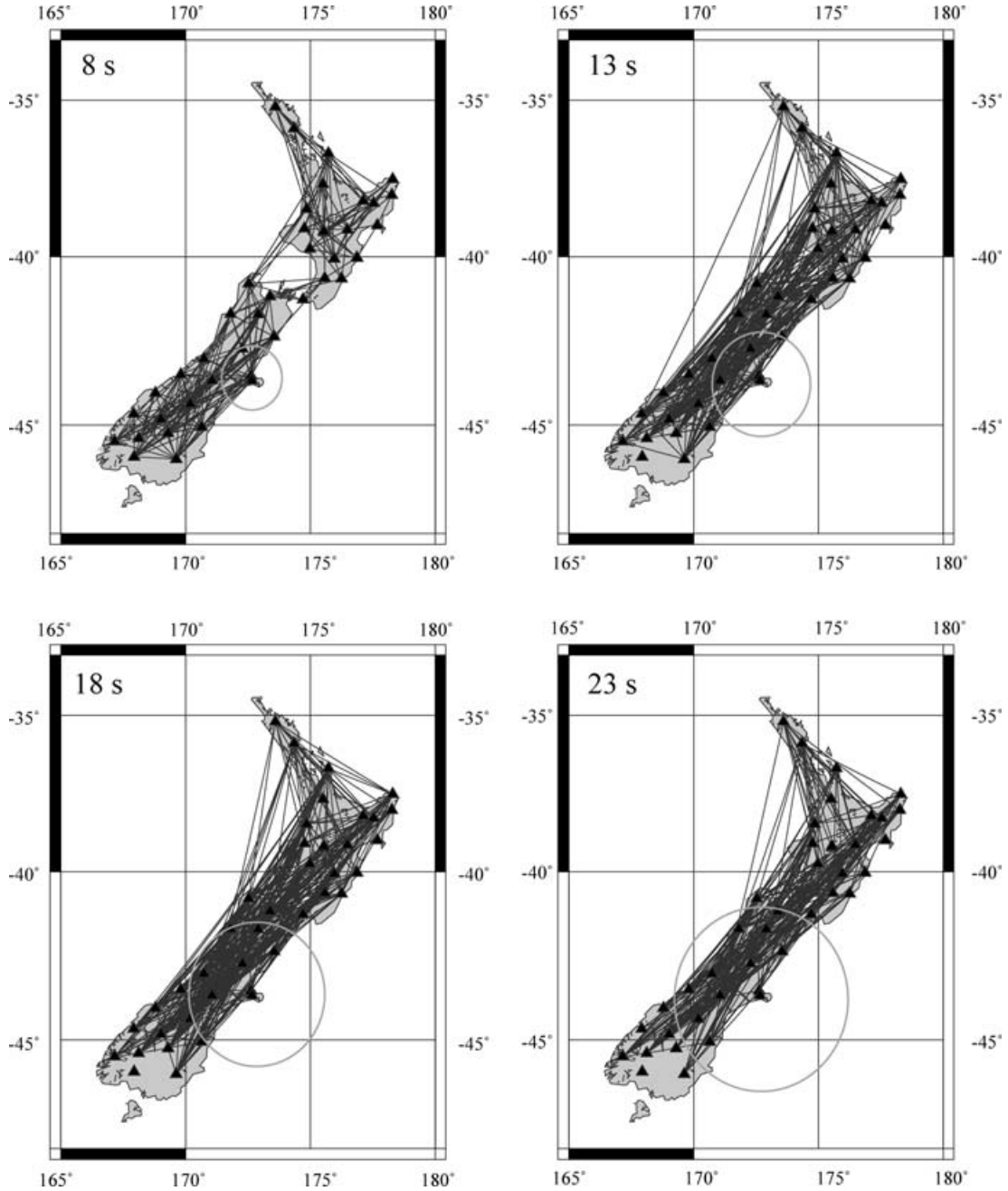

Figure 9 The interstation paths for all the group speed measurements meeting the selection criteria at periods of 8, 13, 18 and 23 s. The circle in each map has radius equal to three wavelengths. Hence, for a station at the centre of the circle, the enclosed area is the region too close to pass the first selection criterion.

Fig. 13), Fiordland and Otago. In northwest Nelson and Fiordland these higher velocities correspond approximately to the mapped locations of the Median Batholith (Mortimer 2004), and appear to be restricted to the northern side of the Wairau Fault. We note that high velocities are also seen in Marlborough and Cook Strait, where they are possibly associated with Haast schist.

5.1.4 23 s group velocities

Compared to the shorter-period maps, the 23 s map reveals only large features oriented along the strike of the islands. This is straightforwardly interpreted as the effect of sampling bias, because all the paths satisfying the first selection criterion in Section 3 need to be longer than ∼275 km (Fig. 9). Most of the measurements used to produce this map not only span long paths but also have a strong azimuthal bias. Thus, the 23 s map only represents large-scale averages, and illustrates little local detail. The depth extent of the velocity information that results is similarly limited, as discussed further in the next section.

5.2 1-D shear velocity models

Here, we present four characteristic 1-D isotropic shear velocity models based on the 7–25 s tomography maps. These simplified models are designed to show broad features of the data and how they might be represented by velocity changes with depth. Tomographic

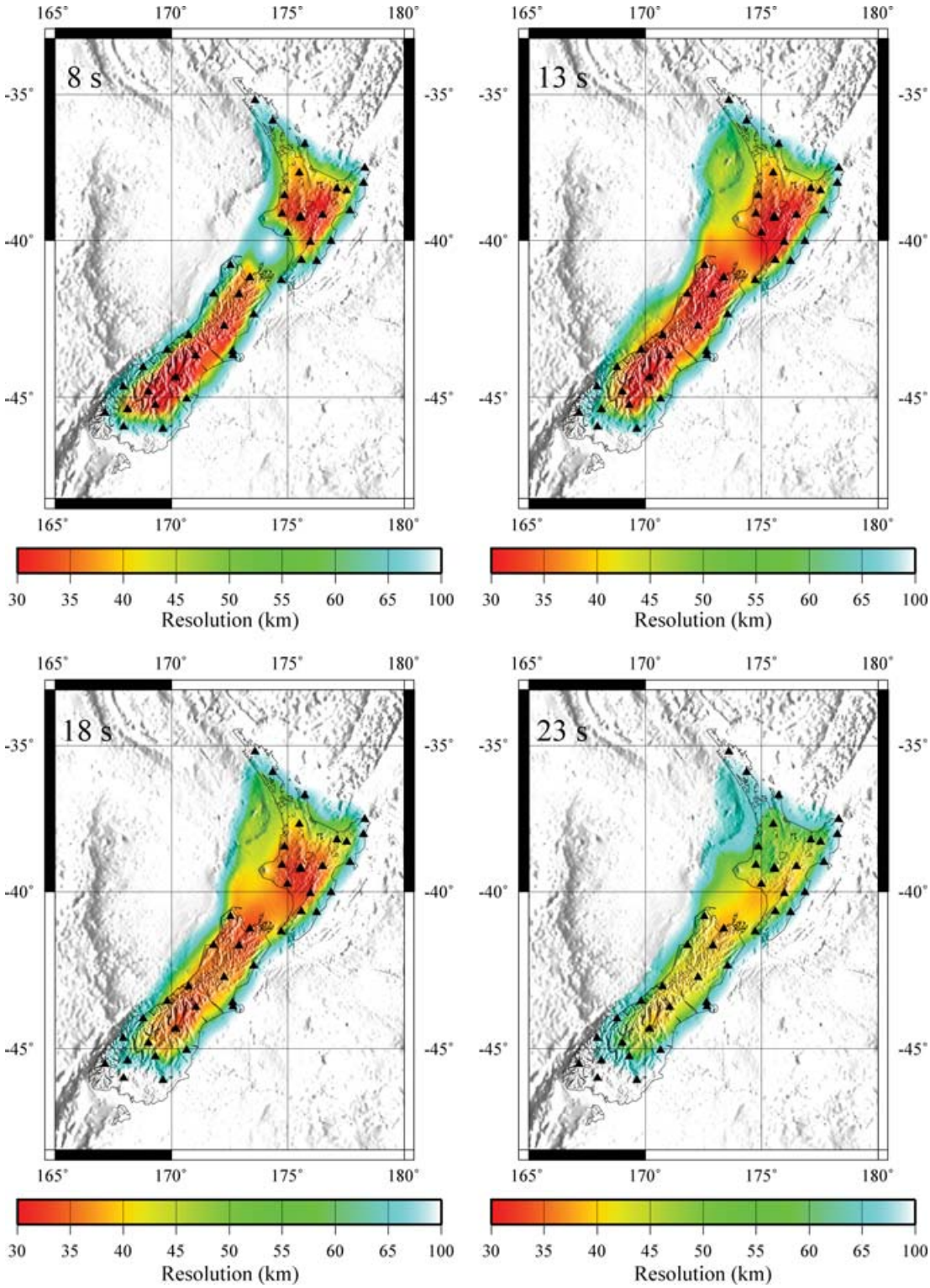

Figure 10 Estimated resolution at periods of 8, 13, 18 and 23 s. Resolution is defined as the standard deviation of the Gaussian fit to the resolution map at each model node (defined in km). Warm colours indicate areas of high resolution.

inversion for 3-D structure is an important goal for further work. Two points in the North Island and two points in the South Island (Fig. 5a) are chosen for this purpose. For each point, the group velocities from the four adjacent grid points are taken from each tomography map, to yield the dispersion curve assigned to the central point (Fig. 14a), and the spread of measurements that govern the inversion. A Monte Carlo method similar to that used by Shapiro & Ritzwoller (2002) is then applied to obtain the 1-D shear velocities profile providing the best fit to the dispersion curve given its associated uncertainties (Fig. 14b).

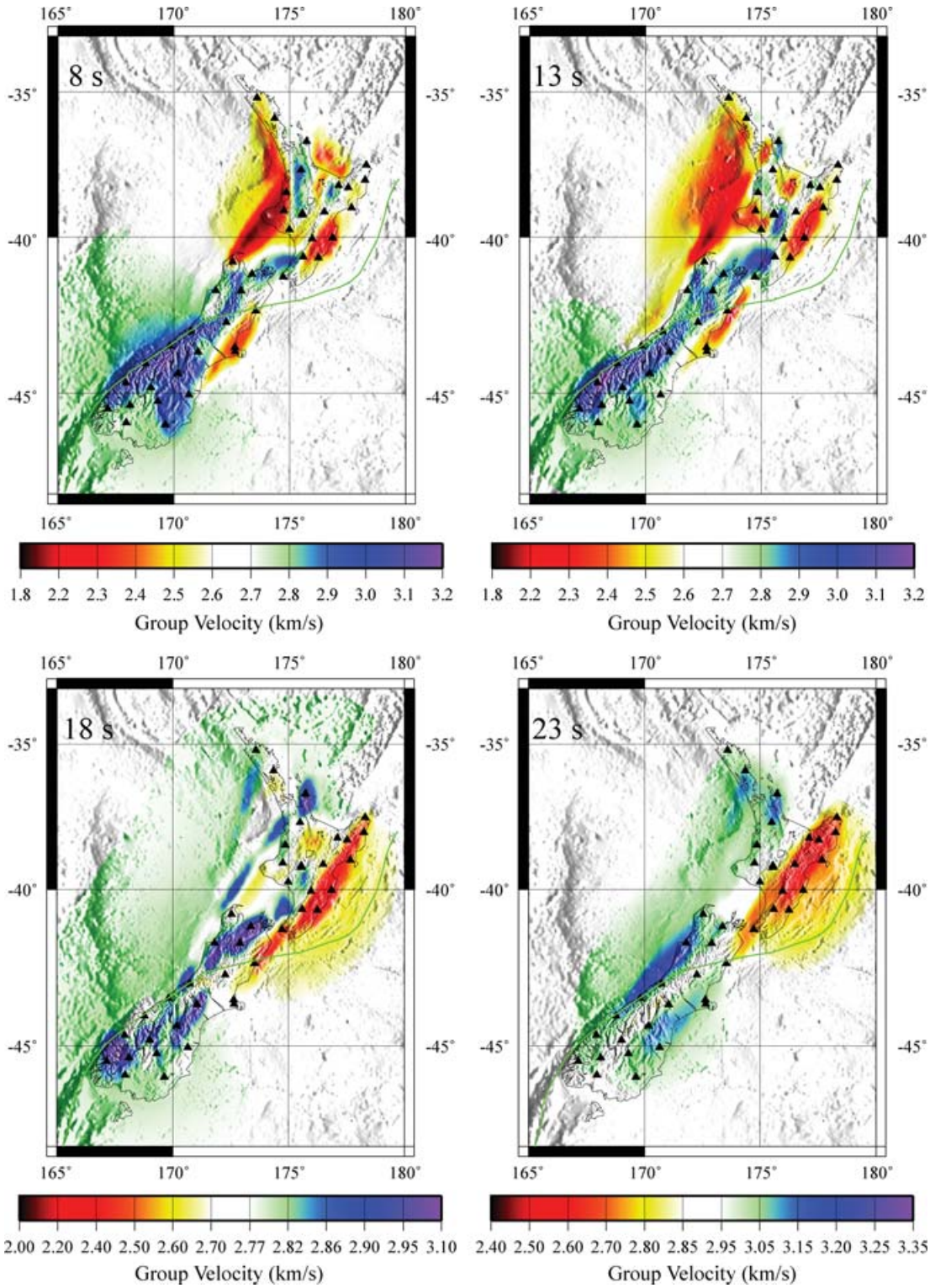

Figure 11 The estimated group velocity maps at periods of 8, 13, 18 and 23 s. Note that the smearing effect off-shore with no path coverage is due to the contrast between the on-shore velocity and the reference velocity.

In the inversion, we parametrize the model to include four crustal layers and a single mantle layer. Because Rayleigh waves are more sensitive to shear velocities than compressional velocities, we fix the V_p/V_s ratio of each layer but allow its shear velocity and thickness to vary randomly during the Monte Carlo search. In addition, because the dispersion curve between 7 and 25 s periods only weakly constrains either the top few kilometres of the crust or the structure deeper than about 30 km, we fix the shear velocity in the uppermost crustal layer and the mantle to be 2.55 and 4.4 km s^{-1}, respectively. We also impose a monotonicity constraint on the velocities in order

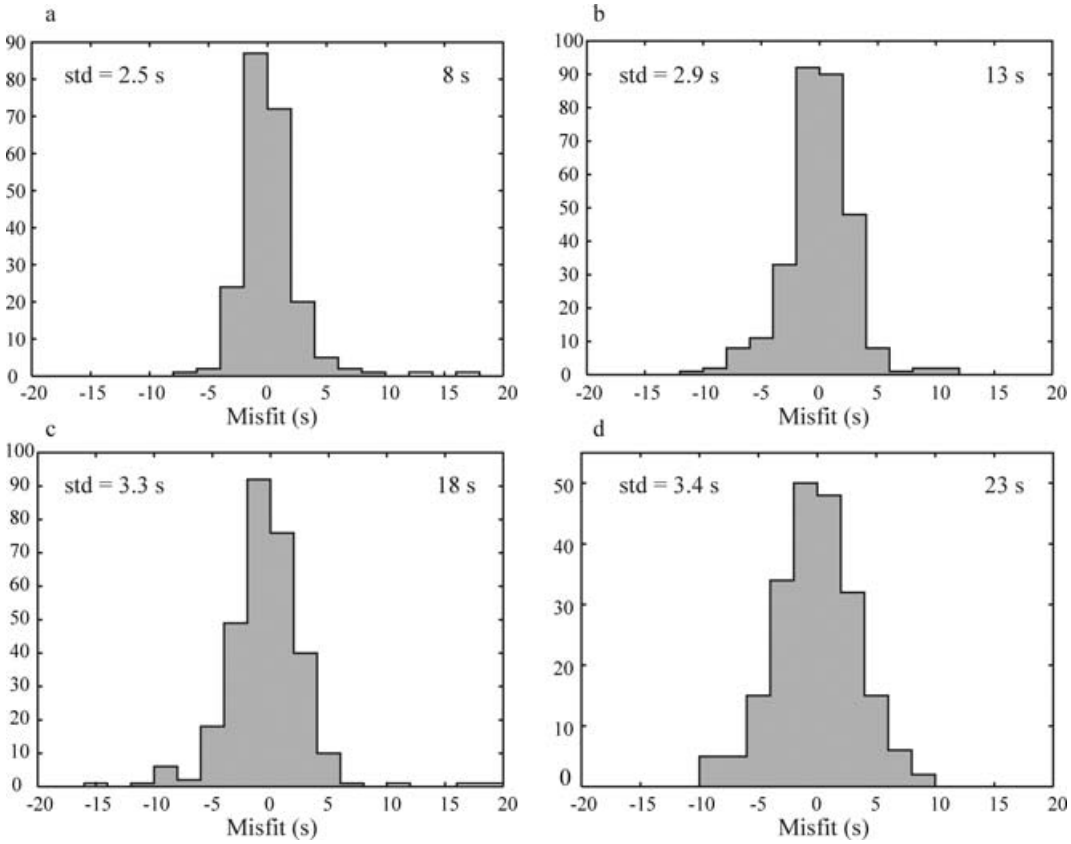

Figure 12 Histograms of traveltime misfit after tomography at periods of 8, 13, 18 and 23 s. The standard deviation (std) of the misfit is also shown.

to obtain a physically plausible model: that is, velocities must satisfy $m_i < m_{i+t}$ where m_i is the velocity of a layer directly over a layer with velocity m_{i+1}.

The best-fitting profiles at each of the four locations are shown in Fig. 14(b). Although a range of models will fit the data and *a priori* constraints acceptably, several aspects of the best-fitting profiles are worth mentioning. First, compared to the other regions, the Southern Alps point has the thinnest top layer, which is presumably because of the lack of sediments. In contrast, the Canterbury Basin profile has the thickest top layer which accurately reflects the thickest sedimentary deposits there relative to the other three points. Second, shear velocities are fairly constant down to ∼35 km for the Southern Alps profile. This is strikingly similar to the V_p model of Scherwath *et al.* (2003) in the same region. Their model has V_p values of 5.6–6.2 km s^{-1} between depths of 3 km and ∼30 km. If we adopt a V_p/V_s ratio of 1.73, the corresponding V_s values are 3.24–3.58 km s^{-1} and compare very well with the values of 3.34–3.58 km s^{-1} obtained in the current study (Fig. 14b). Third, with group velocities only measurable to periods of approximately 25 s, crustal thickness trades off strongly with mantle velocity if the crust is thicker than about 30 km. For this reason, we can say little with confidence about crustal thickness on the basis of the noise correlation analysis performed to date, other than that the crust beneath the Southern Alps is thicker than elsewhere. The value of 35 km for the Southern Alps crustal thickness depends strongly on the mantle velocity chosen so should not be interpreted quantitatively.

We have also inverted the two observed dispersion curves shown in Fig. 5 for the paths through the Southern Alps and the Canterbury Basin. The advantage of these inversions is that the measured curves extend to longer periods than those constructed from the dispersion maps and, therefore, constrain structures to greater depth. Inversion of the measured curves reveals similar crustal structure and thickness, but tightens the constraint on the shear velocity of uppermost mantle. The shear velocity of the uppermost mantle beneath the Southern Alps, consistent with the measured curve, is 4.19 km s^{-1}, and beneath the Canterbury Basin is 4.51 km s^{-1}. These values can be contrasted with 4.4 km s^{-1}, which is imposed on the inversion of the curves from the dispersion maps. However, there is likely still some trade-off between mantle velocity and crustal thickness under the Southern Alps, as thicknesses of almost 50 km have been measured from earthquake refraction profiling (Bourguignon *et al.* 2007).

We wish to emphasize that these best fitting 1-D models are intended only to provide a flavour of future research and any quantitative interpretation needs to be made with caution. In order to constrain the crustal structure better, more detailed studies are needed which include quantifying the range of models that give the dispersion curves within the uncertainty. To further improve the credibility of the velocity models, joint inversion between ambient-noise surface wave measurements, receiver functions, and teleseismic measurements are needed. However, these are beyond the scope of this study.

5.3 Azimuthal distribution of ambient noise sources

The cross-correlation results not only contain information about the speed of wave propagation between pairs of stations (i.e. the Rayleigh wave speeds at different frequencies), but also information about the azimuthal distribution of the source(s) of the ambient noise itself. A comparison of the positive and negative lags of the

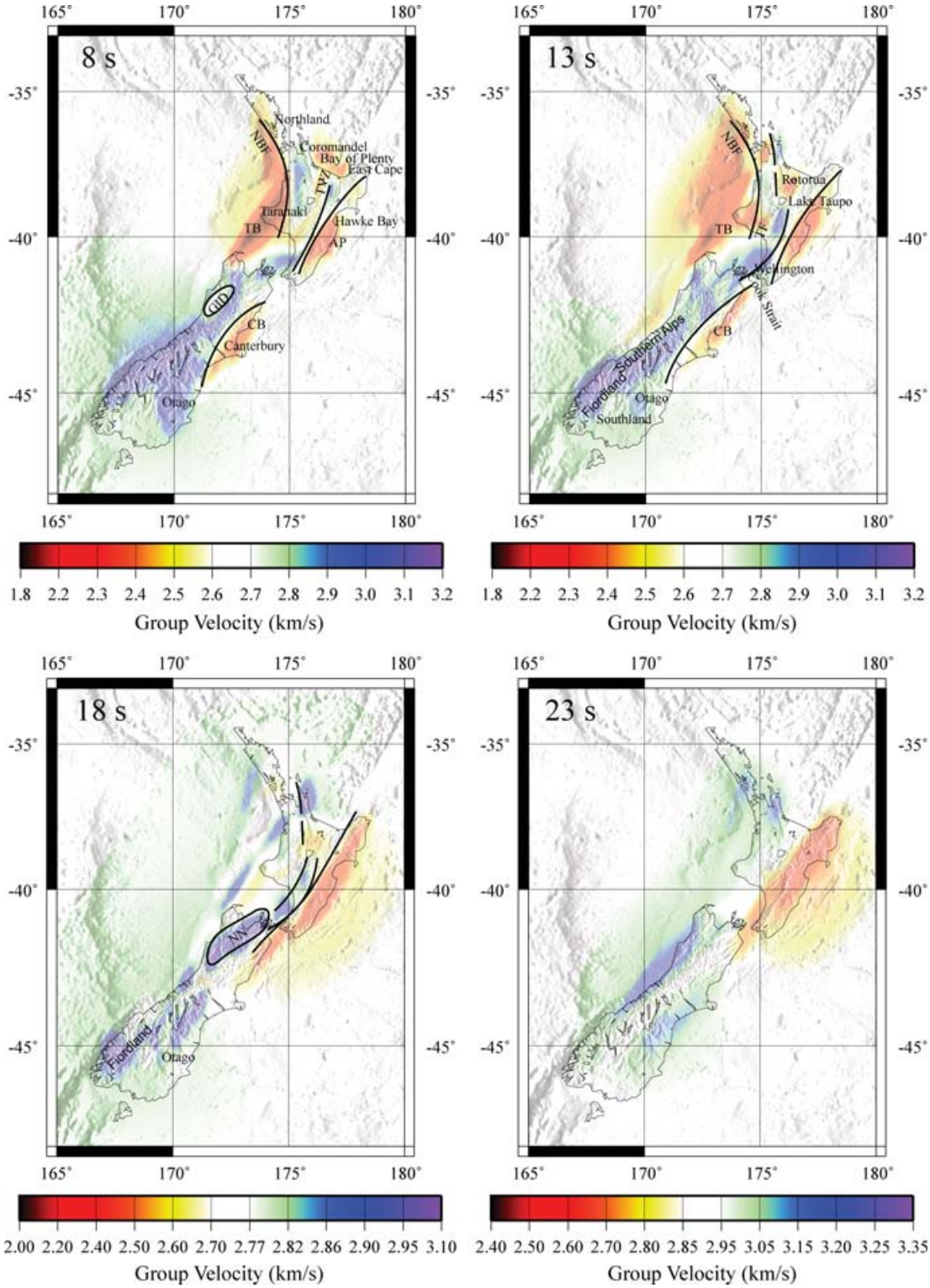

Figure 13 Interpretation of the group velocity maps. Refer to text for the abbreviations.

cross-correlation time-series provides some insight into the relative strength of the waves propagating in opposite directions. We present here a brief analysis of the noise directionality based on a single 12-month stack: this yearly average may mask any seasonable variability, which is the subject of on-going research using longer records.

We separately calculate the SNR spectrum for the positive- and negative-lag components of the cross-correlation between each station-pair and multiply that by the square root of the distance between the two stations to compensate for geometrical spreading. Fig. 15 summarizes the results for the four periods shown in the tomographic maps of Fig. 11. For each pair of stations, two arrows

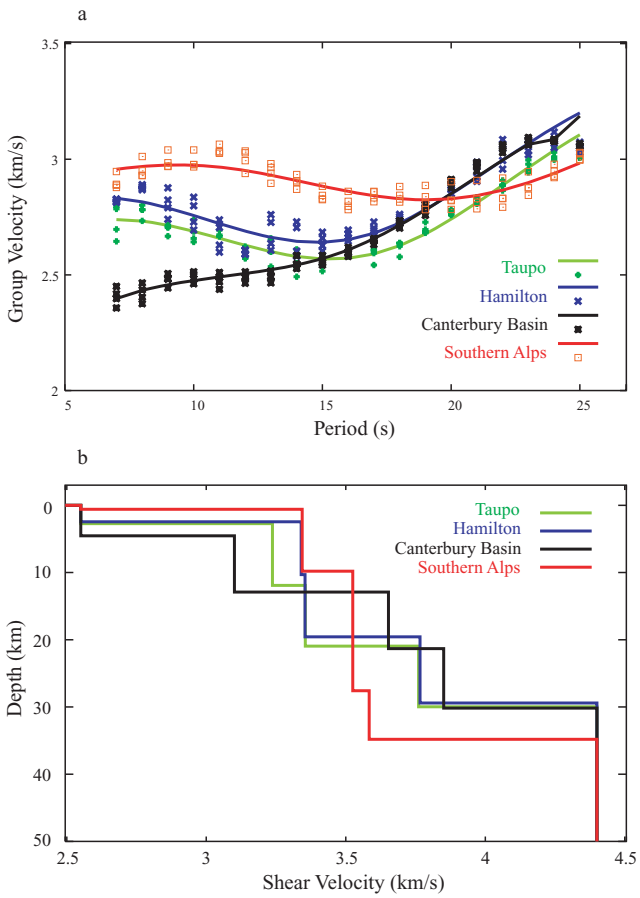

Figure 14 (a) The group velocity measurements at four positions (Taupo green, Hamilton blue, Canterbury Basin black and Southern Alps red). At each position four measurements are taken from the tomography maps. The smooth lines represent the best fitting dispersion curves from the 1-D model in (b). The colour codes in (a) and (b) are the same.

with opposite directions are plotted at each station. The length of each arrow is proportional to the SNR multiplied by the square root of the distance and the direction of the arrow represents the direction of wave propagation. We restrict the calculation to pairs of stations separated by a distance in kilometres larger than six times the period in seconds, rather than the twelve times used in the first selection criterion discussed in Section 3. This is because the effect of overlap between the positive- and negative-lags on the noise directivity estimates is minor compared to group velocity measurement, which is sensitive to small variations.

Several conclusions can be drawn from these maps. At 8 s and 13 s periods, the South Island exhibits generally stronger and more coherent signals than the North Island. The signals at 8 s predominantly arrive from the south, southwest and southeast quadrants in the South Island, whereas in the North Island they are more azimuthally uniform. Short-period energy arriving from the north appears to be minimal at South Island stations. These observations are consistent with oceanographic data, which reveal that the high-energy west, south and east coasts of New Zealand have predominant wave heights and periods of 1–3 m and 6–8 s, ∼4 m and 10–12 s, and 0.5–2 m and 7–11 s, respectively (Pickrill & Mitchell 1979). In contrast, the low-energy north coast (between North Cape and East Cape) experiences a prevailing northeasterly swell with 0.5–1.5 m wave heights and 5–7 s wave periods.

At periods of 13, 18 and 23 s, stations TOZ, KNZ and WHZ exhibit only weak signals and are revealed by ambient noise level analysis (*cf.* Lin *et al.* 2006) to suffer from high local noise. The broadband sensor at each of these sites is a Guralp CMG-40T, which has poorer SNR characteristics than the newer Guralp CMG-3ESP and Streckheisen STS-2 sensors used elsewhere (K. Gledhill, personal communication 2006).

For periods greater than 13 s, strong waves appear to arrive preferentially from the northeast and southwest. The >150 km-long paths over which these measurements are made tend to be oriented parallel to the overall strike of New Zealand, particularly in the South Island. It is difficult, therefore, at these longer periods to infer the azimuthal distribution of the incoming waves given highly biased sampling. For this reason, we believe that only the 8 s data adequately represent the azimuthal variability of the incoming noise.

6 CONCLUSIONS

We present here the first New Zealand-wide study of surface wave dispersion, using ambient noise recordings at 42 broad-band stations. By correlating year-long time series between stations, we have obtained Rayleigh wave group velocity dispersion curves and estimated their associated uncertainties based on seasonal variability. Group velocity maps calculated at periods of 8–23 s reveal a close correlation between Rayleigh wave group velocity and major geological features: in particular, the major sedimentary basins are clearly imaged at 8–18 s periods, and a number of previously reported boundaries between basement terranes in central New Zealand are also manifest at these periods. We have also constructed four 1-D shear velocity models to illustrate the vertical resolution obtainable with these measurements.

At periods longer than approximately 20–25 s, in particular, it is clear that constraints imposed on the seismic network by New Zealand's long, narrow geometry impose limitations on surface wave analysis and the analysis of structure deeper than approximately 30 km. In order to image better New Zealand's deeper structure using these techniques, broad-band ocean bottom seismometers (OBSs) deployed on the continental shelf appear necessary. OBS arrays deployed on either side of the country would improve both the number of paths along which long-period measurements can be made and the azimuthal distribution of those paths.

This study is intended to serve as a foundation for several lines of future research. Among these are the use of horizontal-component seismograms (which would enable Love waves to be analysed), measurement of phase velocity of both Rayleigh and Love waves, and cross-correlation amongst local network stations at frequencies perhaps as high as 1 Hz. Ongoing research will make use of longer-duration data sets and data acquired with new broadband seismometers installed in the far south of the South Island in early 2006 as part of GeoNet's ongoing expansion, augmented with data recorded during short-term deployments. This will improve the propagation path coverage and long-period SNR characteristics of the group velocity measurements, and enable us to perform 3-D anisotropic shear wave velocity tomography.

ACKNOWLEDGMENTS

The authors gratefully acknowledge the New Zealand GeoNet Project (http://www.geonet.org.nz) and the IRIS Data Management Center for access to the data on which this research is based. We particularly thank Mark Chadwick and Ken Gledhill, GNS Science,

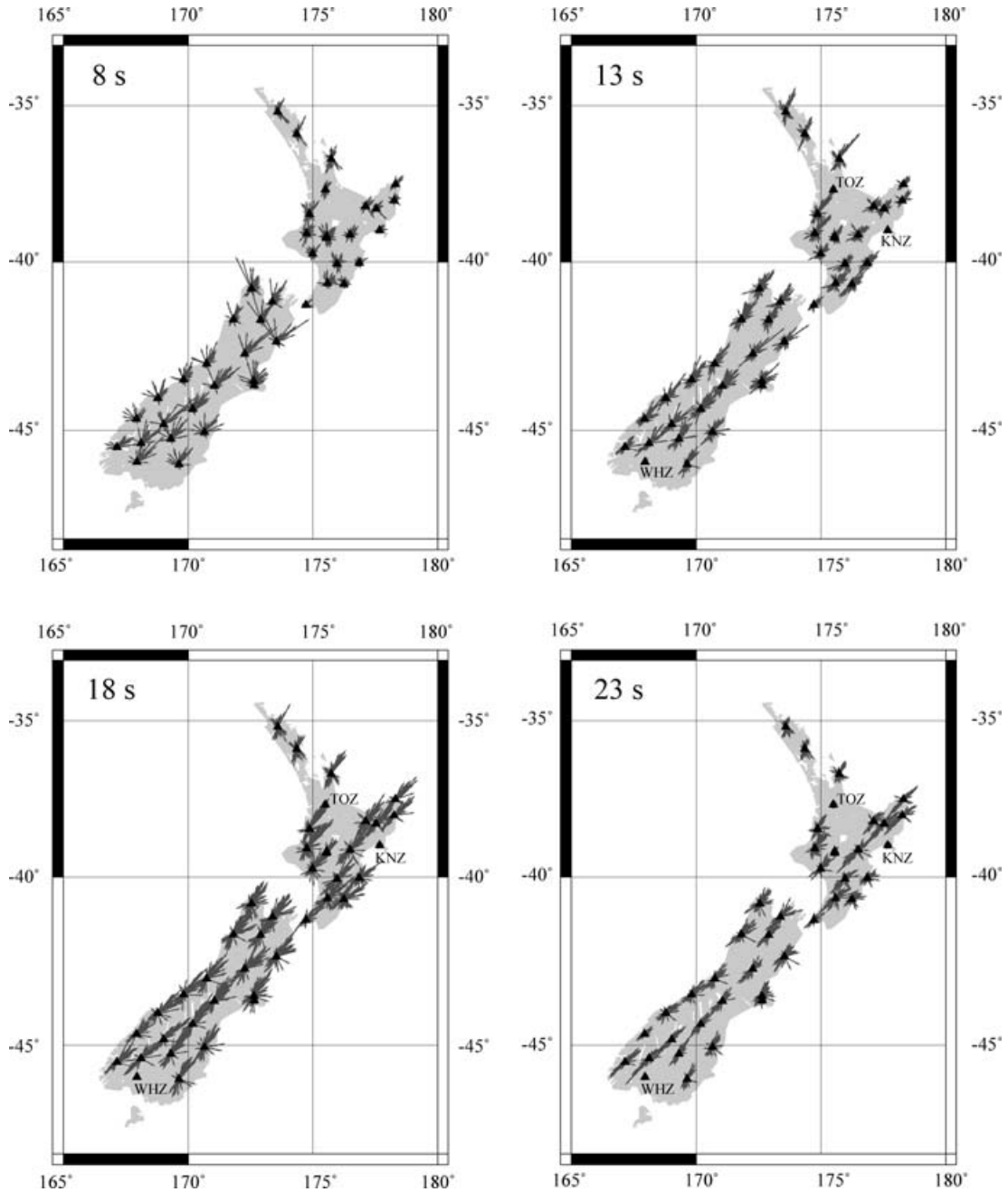

Figure 15 Summary of ambient noise directionality at periods of 8, 13, 18 and 23 s. For each station pair separated by more than 1.5 wavelengths two arrows with opposite directions are plotted at each station. The length of each arrow is proportional to the SNR at positive or negative lag (whichever is appropriate) multiplied by the square root of the interstation distance. The arrows point along the great-circle linking the stations in the direction toward which the energy propagates. For example, energy propagating from the south will be represented by a northward pointing arrow. Three stations TOZ, KNZ and WHZ with high local noise are also shown on the maps.

for help with obtaining GeoNet data and discussions regarding the SNR characteristics of different GeoNet instruments. Comments from Lapo Boschi, Fred Davey, and two anonymous reviewers are appreciated and helped to improve this paper. We also thank Indrajit Das, Indian Institute of Technology at Kharagpur, for help in implementing the noise correlation algorithms at VUW during a short-term internship. This work was undertaken with support from the Foundation for Research, Science and Technology and the VUW Institute of Geophysics, School of Geography, Environment and Earth Sciences.

REFERENCES

Anderson, H.J., 1979. A geophysical study of the Westport, Inangahua and Murchison Basins, West Coast, South Island, *Geophysics Division, Department of Scientific and Industrial Research, Research Report,* **148,** 53 p.

Ansell, J.H. & Bannister, S., 1996. Shallow morphology of the subducted Pacific plate along the Hikurangi margin, New Zealand, *Phys. Earth. Planet. In.,* **93,** 3–10.

Baldock, G. & Stern, T., 2005. Width of mantle deformation across a continental transform: evidence from upper mantle (Pn) seismic anisotropy measurements, *Geology,* **33**(9), 741–744.

Barmin, M.P., Ritzwoller, M.H. & Levshin, A.L., 2001. A fast and reliable method for surface wave tomography, *Pure Appl. Geophys.,* **158,** 1351–1375.

Beanland, S., Melhuish, A., Nicol, A. & Ravens, J., 1998. Structure and deformational history of the inner forearc region, Hikurangi subduction margin, New Zealand, *New Zeal. J. Geol. Geophys.,* **41,** 325–342.

Bensen, G.D., Barmin, M.P., Levshin, A.L., Lin, F., Moschetti, M.P., Shapiro, N.M., Yang, Y. & Ritzwoller, M.H., 2007. Processing ambient noise seismic data to obtain reliable broadband surface wave dispersion measurements, doi: 10.1111/j.1365-246X.2007.03374.x, *Geophys. J. Int.,* submitted.

Bourguignon, S., Stern, T.A. & Savage, M.K., 2007. Crust and mantle thickening beneath the southern portion of the Southern Alps, New Zealand, *Geophys. J. Int.,* **168,** 681–690.

Brisbourne, A.M. & Stuart, G.W., 1998. Shear-wave velocity structure beneath North Island, New Zealand, from Rayleigh-wave interstation phase velocities, *Geophys. J. Int.,* **133,** 175–184.

Brisbourne, A., Stuart, G. & Kendall, J.-M., 1999. Anisotropic structure of the Hikurangi subduction zone, New Zealand —integrated interpretation of surface-wave and body-wave observations, *Geophys. J. Int.,* **137,** 214–230.

Butler, R. *et al.*, 2004. Global seismographic network surpasses its design goal, *Eos Trans. AGU,* **85**(23), 225.

Cho, K.H., Hermann, R.B., Ammon, C.J. & Lee, K., 2007. Imaging the upper crust of the Korean Peninsula by surface-wave tomography, *Bull. Seism. Soc. Amer.,* **97,** 198–207.

Campillo, M. & Paul, A., 2003. Long-range correlations in the diffuse seismic coda, *Science,* **299,** 547–549.

Dahlen, F.A. & Zhou, Y., 2006. Surface wave group delay and attenuation kernels, *Geophys. J. Int.,* **165,** 545–554.

Davey, F.J. & Broadbent, M., 1980. Seismic refraction measurements in Fiordland, southwest New Zealand, *New Zeal. J. Geol. Geophys.,* **23,** 395–406.

Davey, F. J., Henrys, S. A. & Lodolo, E., 1995. Asymmetric rifting in a continental back-arc environment, North Island, New Zealand, *J. Volcanol. Geoth. Res.,* **68,** 209–238.

Davey, F.J., Hampton, M., Childs, J., Fisher, M.A., Lewis, K. & Pettinga, J.R., 1986. Structure of a growing accretionary prism, Hikurangi Margin, *New Zealand. Geol.,* **14,** 663–666.

Davey, F.J. *et al.*, 1998. Preliminary results from a geophysical study across a modern continent-continent collisional plate boundary — The Southern Alps, New Zealand, *Tectonophysics,* **288,** 221–235.

Derode, A., Larose, E., Tanter, M., de Rosny, J., Tourim, A., Campillo, M. & Fink, M., 2003. Recovering the Green's function from filed-field correlations in an open scattering medium (L), *J. Acoust. Soc. Am.,* **113,** 2973–2976.

Eberhart-Phillips, D. & Bannister, S., 2002. Three-dimensional crustal structure in the Southern Alps region of New Zealand from inversion of local earthquake and active source data, *J. Geophys. Res.,* **107,** 2262.

Eberhart-Phillips, D. & McVerry, G., 2003. Estimating slab earthquake response spectra from a 3D Q model, *Bull. Seismol. Soc. Am.,* **93,** 2649–2663.

Godfrey, N.J., Davey, F.J., Stern, T.A. & Okaya, D., 2001. Crustal structure and thermal anomalies of the Dunedin region, South Island, New Zealand, *J. Geophys. Res.,* **106,** 30 835–30 848.

Godfrey, N.J., Christensen, N.I. & Okaya, D.A., 2002. Anisotropy of schists: contribution of crustal anisotropy to active source seismic experiments and shear wave splitting observations, *J. Geophys. Res.,* **105,** 27 991–28 007.

Gorman, R.M., Bryan, K. & Laing, A.K., 2003. Wave hindcast for the New Zealand region: nearshore validation and coastal wave climate, *New Zeal. J. Mar. Freshwat. Res.,* **37,** 567–588.

Harrison, A.J. & White, R.S., 2004. Crustal structure of the Taupo Volcanic Zone, New Zealand: stretching and igneous intrusion, *Geophys. Res. Lett.,* **13,** L13615, 1–4.

Hatherton, T., 1970. Upper mantle inhomogeneities beneath New Zealand: surface manifestations, *J. Geophys.Res.,* **75,** 269–84.

Henrys, S., Reyners, M., Pecher, I., Bannister, S., Nishimura, Y. & Maslen, G., 2006. Kinking of the subducting slab by escalator normal faulting beneath the North Island of New Zealand, *Geology,* **34,** 777–780.

Horspool, N.A., Savage, M.K. & Bannister, S., 2006. Implications for intraplate volcanism and back-arc deformation in northwestern New Zealand, from joint inversion of receiver functions and surface waves, *Geophys. J. Int.,* **166,** 1466–1483.

King, P.R. & Thrasher, G.P., 1996. Cretaceous-Cenozoic geology and petroleum systems of the Taranaki Basin, New Zealand. Lower Hutt: Institute of Geological & Nuclear Sciences, *Inst. Geol. Nucl. Sci. Monogr.,* **13,** 243 p.

Laing, A.K., 2000. New Zealand wave climate from satellite observations, *New Zeal. J. Mar. Freshwat. Res.,* **34,** 745–749.

Larose, E., Derode, A., Corennec, D., Margerin, L. & Campillo, M., 2005. Passive retrieval of Rayleigh waves in disordered elastic media, *Phys. Rev. E.,* **72,** 046607, doi:10.113/PhysRevE.72.046607.

Levshin, A.L. & Ritzwoller, M.H., 2001. Automated detection, extraction, and measurement of regional surface waves, *Pure Appl. Geophys.,* **158,** 1531–1545.

Levshin, A.L., Barmin, M.P., Ritzwoller, M.H. & Trampert, J., 2005. Minor-arc and major-arc global surface wave diffraction tomography, *Phys. Earth Planet. Int.,* **149,** 205–223.

Lin, F., Ritzwoller, M.H. & Shapiro, N.M., 2006. Is ambient noise tomography across ocean basins possible? *Geophys. Res. Lett.,* **33,** L14304, doi:10.1029/2006GL026610.

Mooney, H., 1970. Upper mantle inhomogeneity beneath New Zealand: seismic evidence, *J. Geophys. Res.,* **75,** 285–309.

Mortimer, N., 1993. Metamorphic zones, terranes and Cenozoic faults in the Marlborough Schist, New Zealand, *New Zeal. J. Geol. Geophys.,* **36,** 357–368.

Mortimer, N., Tulloch, A.J. & Ireland, T.R., 1997. Basement geology of Taranaki and Wanganui Basins, New Zealand, *New Zeal. J. Geol. Geophys.,* **40,** 223–236

Mortimer, N., 2004 New Zealand's geological foundations, *Gondwana Res.,* **7**(1), 261–272

Moschetti, M.P., Ritzwoller, M.H. & Shapiro, N.M., 2005. California surface wave tomography from ambient seismic noise: Tracking the progress of the USArray Transportable Network, *Eos Trans. AGU,* **86**(52), Fall Meet. Suppl., Abstract S31A-0276.

Okaya, D., Henrys, S. & Stern, T., 2002. Double-sided onshore-offshore seismic imaging of a plate boundary: "super-gathers" across South Island, New Zealand, *Tectonophysics,* **355,** 247–263.

Paul, A., Campillo, M., Margerin, L., Larose, E. & Derode, A., 2005. Empirical synthesis of time-asymmetrical Green functions from the correlation of coda waves, *J. Geophys. Res.,* **110,** B08302, doi:10.1029/2004JB003521.

Pickrill, R.A. & Mitchell, J.S., 1979. Ocean wave characteristics around New Zealand, *New Zeal. J. Mar. Fresh. Res.,* **13,** 501–520.

Reyners, M., Eberhart–Phillips, D., Stuart, G. & Nishimura, Y., 2006. Imaging subduction from the trench to 300 km depth beneath the central North Island, New Zealand, with Vp and Vp/Vs, *Geophys. J. Int.,* **165**(2), 565–583.

Ritzwoller, M.H. & Levshin, A.L., 1998. Eurasian surface wave tomography: group velocities, *J. Geophys. Res.,* **103,** 4839–4878.

Ritzwoller, M.H., Shapiro, N.M., Barmin, M.P. & Levshin, A.L., 2002. Global surface wave diffraction tomography, *J. Geophys. Res.,* **107**(B12), 10.1029/2002JB001777.

Roux, P., Sabra, K.G., Gerstoft, P., Kuperman, W.A. & Fehler, M.C., 2005. P-waves from cross-correlation of seismic noise, *Geophys. Res. Lett.,* **32,** L19393, doi:10.1029/2005GL023803.

Sabra, K.G., Gerstoft, P., Roux, P., Kuperman, W.A. & Fehler, M.C., 2005a. Extracting time-domain Green's function estimates from ambient seismic noise, *Geophys. Res. Lett.,* **32,** L03310, doi:10.1029/2004GL021862.

Sabra, K.G., Gerstoft, P., Roux, P., Kuperman, W.A. & Fehler, M.C., 2005b. Surface wave tomography from microseism in southern California, *Geophys. Res. Lett.,* **32,** L14311, doi:10.1029/2005GL023155.

Salmon, M., Bannister, S., Bibby, H., Savage, M.K. & Stern T.A., 2003. Attenuation and electrical resistivity in an asymmetric back arc extensional environment, *Eos Trans. AGU,* **84**(46), Fall Meet. Suppl., Abstract S22B-0450.

Savage, M.K., Fisher, K.M. & Hall, C.E., 2004. Strain modelling, seismic anisotropy, and coupling at strike-slip boundaries: applications in New Zealand and the San Andreas fault, in *Vertical Coupling and Decoupling in the Lithosphere,* pp. 9–40, eds, Grocott, J., Tikoff, B., McCaffrey, K.J.W. & Taylor, G., Geological Society, London.

Scherwath, M. *et al*., 2002. Pn anisotropy and distributed upper mantle deformation associated with a continental transform fault, *Geophys. Res. Lett.,* **29**(8), 16–1.

Scherwath, M., Stern, D., Davey, F., Davies, R., Kleffmann, S. & Okaya, D., 2003. Lithospheric structure across oblique continental collision in New Zealand from wide-angle P-wave modelling, *J. Geophys. Res.,* **108,** 2566, doi:10.1029/2004GL019491.

Shapiro, N.M. & Campillo, M., 2004. Emergence of broadband Rayleigh waves from correlations of the ambient seismic noise, *Geophys. Res. Lett.,* **31,** L07614, doi:10.1029/2004GL019491.

Shapiro, N.M. & Ritzwoller, M.H., 2002. Monte-Carlo inversion for a global shear velocity model of the crust and upper mantle, *Geophys. J. Int.,* **151,** 88–105.

Shapiro, N.M., Campillo, M., Stehly, L. & Ritzwoller, M.H., 2005. High resolution surface wave tomography from ambient seismic noise, *Science,* **307,** 1615–1618.

Sherburn, S., White, R.S. & Chadwick, M., 2006. Three-dimensional tomographic imaging of the Taranaki volcanoes, New Zealand, *Geophys. J. Int.,* **166,** 957–969.

Sieminski, A., Leveque, J.-J. & Debayle, E., 2004. Can finite-frequency effects be accounted for in ray theory surface wave tomography? *Geophys. Res. Lett.,* **31,** L24614, doi:10.1029/2004GL021402.

Snieder, R., 2004. Extracting the Green's function from the correlation of coda waves: a derivation based on stationary phase, *Phys. rev. E,* **69,** 046610.

Spetzler, J., Trampert, J. & Snieder, R., 2002. The effects of scattering in surface wave tomography, *Geophys. J. Int.,* **149,**755–767.

Stern, T.A., 1987. Asymmetric back-arc spreading, heat flux and structure associated with the Central Volcanic Region of New Zealand, *Earth and planet. Sci. Lett.,* **85,** 265–276.

Stern, T., Molnar, P., Okaya, D. & Eberhart-Phillips, D., 2000. Teleseismic P wave delays and modes of shortening the mantle lithosphere beneath South Island, New Zealand, *J. Geophys. Res.,* **105,** 21 615–21 631.

Stern, T.A., Stratford, W.R. & Salmon, M.L., 2006. Subduction evolution and mantle dynamics at a continental margin: Central North Island, New Zealand, *Rev. Geophys.,* **44,** RG4002.

Stern, T.A. & Davey, F.J., 1987. A seismic investigation of the crustal and upper mantle structure within the central volcanic region of New Zealand, *J. Geol. Geophys.,* **30,** 217–231.

Stratford, W.R. & Stern, T.A., 2006. Crust and mantle structure of continental backarc: central North Island, New Zealand, *Geophysical J. Int.,* **166,** 469–484, doi:10.1111/j.1365–246X.2006.02967.x.

Uruski, C.I., Cook, R.A., Herzer, R.H. & Isaac, M.J., 2004. Petroleum geology of the Northland sector of the greater Taranaki Basin, in *New Zealand Petroleum Conference proceedings,* 10 p., Crown Minerals, Ministry of Economic Development, Wellington.

Wapenaar, K., 2004. Retrieving the elastodynamic Green's function of an arbitrary inhomogeneous medium by cross correlation, *Phys. Rev. Lett.,* **93,** 254 301, doi:10.1103/PhysRevLett.93.254301.

Weaver, R.L. & Lobkis, O.I., 2001a. Ultrasonics without a source: Thermal fluctuation correlation at MHZ frequencies, *Phys. Rev. Lett.,* **87,** 134 301.

Weaver, R.L. & Lobkis, O.I., 2001b. On the emergence of the Green's function in the correlations of a diffuse field, *J. Acoust. Soc. Am.,* **110,** 3011–3017.

Weaver, R.L. & Lobkis, O.I., 2004. Diffuse fields in open systems and the emergence of the Green's function, *J. Acoust. Soc. Am.,* **116,** 2731–2734.

Wood, R. & Woodward, D., 2002. Sediment thickness and crustal structure of offshore western New Zealand from 3D gravity modelling. *New Zeal. J. Geol. Geophys.,* **45,** 243–255.

Yang, Y., Ritzwoller, M.H., Levshin, A.L. & Shapiro, N.M., 2007. Ambient noise Rayleigh wave tomography across Europe, *Geophys. J. Int.,* **168,** 259–274.

Yao, H., Van Der Hilst, R.D. & de Hoop, M.V., 2006. Surface-wave tomography in SE Tibet from ambient seismic noise and two-station analysis: I. — Phase velocity maps, *Geophys. J. Int.,* **166,** 732–744.

Yoshizawa, K. & Kennett, B.L.H., 2002. Determination of the influence zone for surface wave paths, *Geophys. J. Int.,* **149,** 440–453.

Zhou, Y., Dahlen, F.A. & Nolet, G., 2004. 3-D sensitivity kernels for surface-wave observables, *Geophys. J. Int.,* **158,** 142–168.